Optical techniques for near-wall phenomena in nucleate boiling

Cassiano Tecchio, Benjamin Cariteau, Gilbert Zalczer, Simon Vassant, Pere Roca I Cabarrocas, Pavel Bulkin, Jérôme Charliac, Vadim Nikolayev

OPTICAL TECHNIQUES FOR NEAR-WALL PHENOMENA IN NUCLEATE BOILING

C. Tecchio[1], B. Cariteau[1], G. Zalczer[2], S. Vassant[2], P. Roca i Cabarrocas[3], P. Bulkin[3], J. Charliac[3] and V. Nikolayev[2]

[1]STMF, CEA, Université Paris-Saclay, 91191 Gif-sur-Yvette Cedex, FRANCE.
[2]SPEC, CEA, CNRS, Université Paris-Saclay, 91191 Gif-sur-Yvette Cedex, FRANCE.
[3]LPICM, CNRS, Institut Polytechnique de Paris, Ecole Polytechnique, 91120 Palaiseau, FRANCE.

(E-mail: cassiano.tecchio@cea.fr)

ABSTRACT

We report an experimental method consisting of high-speed and high-resolution optical techniques to investigate the near-wall phenomena in nucleate pool boiling. Our focus is on the micrometric liquid layer (microlayer) that can be formed between the wall and the vapor-liquid interface during the bubble growth. We also investigate the wall dewetting dynamics: the dry spot spreading. The installation performs simultaneous and synchronous measurements of the microlayer thickness profile, the wall temperature distribution and the bubble macroscopic shape by white-light interferometry, infrared thermography and sidewise shadowgraphy, respectively, at 4000 frames per second. The novelty is the white light interferometry, which provides precise data on microlayer thickness. The calibration and validation procedures of these optical techniques are discussed along with the post-processing techniques used for image treatment. We also show the results obtained for a nucleate boiling experiment on single bubble growth. These advanced techniques aim at understanding the fundamental aspects of the near-wall phenomena in nucleate boiling heat transfer, in particular the physics of microlayer formation, its evaporation, the dewetting dynamics and the associated heat transfer. The experimental data can be used to support the development of novel physical models.

KEYWORDS:
Boiling, Bubble, Microlayer, Interferometry, IR thermography, Optics

1. INTRODUCTION

The heat and mass transfer via boiling is involved in a wide range of scientific and industrial applications nowadays, including the steam generation in nuclear power plants. High amounts of energy can be transported by means of phase change without the need of large areas or temperature gradients, making boiling-based equipment compact, cheaper and highly efficient [1, 2]. However, the overall efficiency and safety of such equipment relies on the fundamental understanding of the physical aspects governing the phase change process to generate the steam. Nucleate boiling is a multi-scale phenomenon where bubbles nucleate, grow and interact with each other in a multitude of modes on a time scale of ms. This creates numerous difficulties to observe and understand the physical mechanisms of boiling. Better design specifications and safeguards are required because of this lack of fundamental understanding.

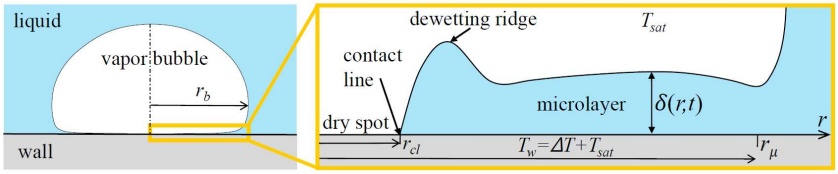

Figure 1. ***Schematics of the near-wall features at bubble growth in nucleate boiling*.**

It is well known from the literature [3, 4, 5] that the phenomena taking place very close to the heater (near-wall phenomena) considerably affect the bubble dynamics and the overall heat transfer performance. In the schematics of Fig. 1, we illustrate two of these phenomena. The first is the dewetting of the wall, i.e. spreading of a dry spot. It is formed in the center of the bubble, which establishes a triple solid-liquid-vapor contact line on the wall. The second is the formation of a micrometric liquid film (microlayer) between the wall and the bubble interface. Because of the low vapor thermal conductivity, the heat flux in the dry spot is very low. Heat accumulates in the dry spot area of the wall, promoting an increase of its temperature. The dewetting mechanism is relevant to the understanding of boiling crisis [2, 3, 6]. Unlike the dry spot, the microlayer acts as a very efficient heat transfer bridge between the wall and the bubble interface (thanks to the low thermal resistance through the microlayer thickness) promoting heat fluxes of the order of MW/m^2 that cool down the wall.

In order to develop high fidelity boiling heat transfer models, high-resolution experiments and precise measurements of these near-wall phenomena are required. In this context, this work reports on the development of novel high-resolution and high-speed optical techniques capable of measuring with precision relevant physical parameters to study the wall dewetting and microlayer dynamics at bubble growth in nucleate boiling.

2. EXPERIMENTAL SETUP: GENERAL OVERVIEW

The experimental installation and the measurement apparatus are schematized in Fig. 1. The experiment is performed in a boiling cell at atmospheric pressure comprising a water liquid pool, a temperature-regulated jacket and a heater. The jacket maintains the pool at a controlled (saturation) temperature thus minimizing thermal gradients in the water. The heater consists of the 1 μm thick indium-tin-oxide (ITO) film deposited on a magnesium fluoride (MgF_2) optical porthole. MgF_2 is transparent to both visible and infrared (IR) light whereas ITO is transparent to visible but opaque to IR waves. The growth of a single bubble at a time is produced by heating up the ITO film locally with the 1.2 μm wavelength IR continuous laser beam of ≈ 1.5 mm diameter. The laser heating mimics a local heating that could occur in the event of a spatially concentrated reaction, for instance.

White light interferometry (WLI), IR thermography (IRT) and sidewise shadowgraphy are set to measure the microlayer thickness δ, wall temperature T_w and macroscopic bubble radius r_b, respectively. The WLI and IRT are performed from below the cell while four lateral transparent portholes provide optical access to the sidewise observation. The WLI works as follows: a collimated white light LED source provides illumination of the bubble foot from below. The visible light beam splitter redirects towards the spectrometer the wave created by light interference at the interfaces between MgF_2, ITO, microlayer and vapor. The light enters the spectrometers through a slit, whose direction defines a scanning line on the heater. Its positioning is adjusted with micrometric stages so it passes through the bubble center. The incoming light is then dispersed into wavelength inside the spectrometer by a diffraction grating. One obtains a spectral fringe map (Fig. 2d) where the vertical and horizontal axes of the image correspond to the wavelength λ and the coordinate r along the scanning line.

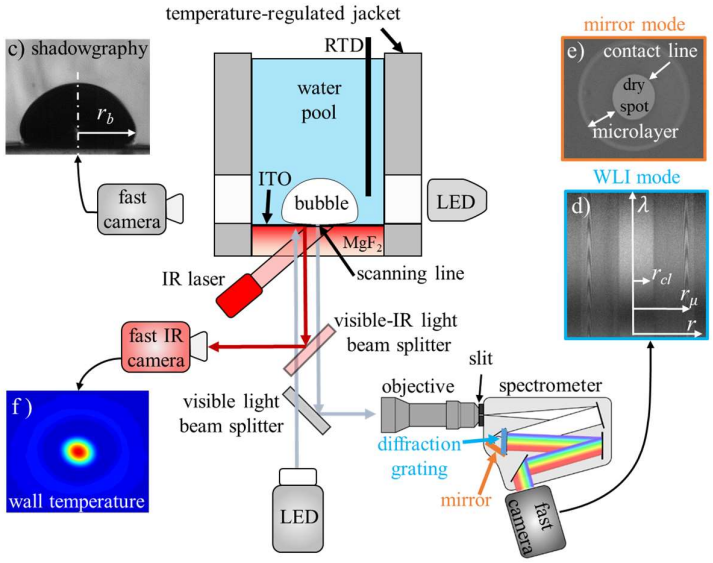

Figure 2. ***Schematics of the experimental pool boiling installation*.**

In Fig. 2d, the extents of dry spot and the microlayer can be observed thanks to the difference in the indexes of refraction of liquid and vapor. The phase distribution on the wall (Fig. 2e) can also be obtained by replacing the diffraction grating by a mirror in the spectrometer. To get δ, one analyzes the spectral fringe map of Fig. 2d as discussed in section 3.3.

The IRT technique is used to measure the temporal evolution of the wall temperature distribution $T_w(x, y, t)$. We use a custom-made multilayer visible-IR light beam splitter (transparent to visible but reflective to IR) positioned between the boiling cell and the visible light beam splitter to reflect the IR waves emitted by the ITO. The reflected IR radiation is captured by the fast IR camera operating in the wavelength range 3-5 μm. The calibration of the IRT technique is presented in section 4. All three cameras record synchronously at 4000 fps.

The core of this experimental installation is the WLI, a novelty in boiling investigations, and the IRT. Therefore, our focus is on description of the calibration and validation of the microlayer thickness and wall temperature measurements. To address the advantages of WLI, we compare our validation results against the classical laser interferometry (LI), widely used in boiling investigations [4, 7, 8, 9, 10]. In the setup of Fig. 2, the LI can be performed by replacing the LED light used for WLI by a monochromatic light source (laser) and use the spectrometer in mirror mode with the slit fully opened.

3. WHITE LIGHT INTERFEROMETRY

3.1. Theory: scalar beam interference model

Figure 3 schematizes the optical path for the transmitted and reflected rays in the heater. Two cases are considered: boiling and validation. In boiling, the media above ITO are the liquid microlayer and vapor. For the validation case, a lens is posed on top of the porthole to create a layer of air. The rays R_1, R_2 and R_3 represent the interfering electromagnetic waves reflected from respective interfaces. The ray R_0 does not interfere with the others because the porthole thickness H is much larger than the length of coherence. Assuming that the incoming light is non-polarized and at normal incidence, there is no effect of polarization upon reflection, and the intensity of the reflected light is [11]

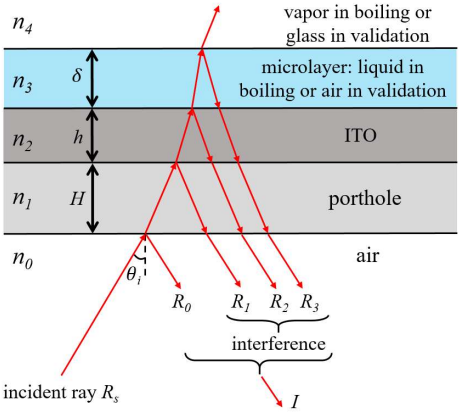

Figure 3. ***Schematics of the light rays in the porthole, ITO and microlayer*.**

$$I = \sum_{i=0}^{3} I_i + \sum_{i=1, j>i}^{3} \left(2\sqrt{I_i I_j} \cos \frac{2\pi \Delta_{ij}}{\lambda} \right) \tag{1}$$

where the indexes i and j correspond to the rays R_i and R_j, respectively. The terms in the second sum in Eq. (1) represent the interference between R_i and R_j. I reaches its maxima and minima when the cosine terms are equal to 1 and -1, representing the constructive and destructive interference, respectively. Δ_{ij} is the path difference between rays R_i and R_j given by

$$\Delta_{ij} = P_{ij} + \Phi_{ij}\lambda \tag{2}$$

which accounts for the contributions of the optical path difference P_{ij} and the phase shifts φ_i and φ_j gained by the rays R_i and R_j at reflection. $\Phi_{ij} = (\varphi_j - \varphi_i)/2\pi$ stands for the net phase shift coefficient. A reflected wave undergoes a $\varphi = \pi$ phase shift when it is reflected from a medium of higher index of refraction, and zero otherwise. At normal incidence ($\theta_i = 0$), one writes [11]

$$P_{12} = 2n_2 h \tag{3}$$

$$P_{23} = 2n_3 \delta \tag{4}$$

$$P_{13} = 2(n_3 \delta + n_2 h) \tag{5}$$

where n_1, n_2 and n_3 represent the indexes of refraction of the porthole, ITO and microlayer. h and δ are the thicknesses of ITO and microlayer, respectively. One can see that this scalar theory corresponds to two-beam interference model that neglects the multiple reflections of beams inside each layer. To evaluate the validity of such an approach, it can be compared to the full electromagnetic theory of interference in multilayer stacks [12]. Figure 4 shows $I(\lambda)$ obtained by the electromagnetic theory and by the scalar interference model given by Eq. (1). A good agreement between both curves is observed for zero net phase shift. Therefore, the simple scalar theory can be used to model the interference.

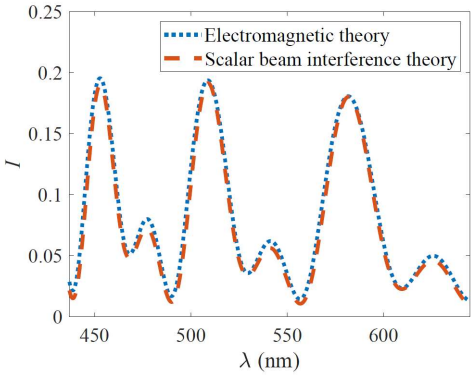

Figure 4. ***Spectral intensity for $h = 850nm$ and $\delta = 1.5\mu m$ for the boiling case. The considered porthole is MgF_2.***

3.2. Calibration

The aim of calibration is to relate the pixel sequential numbers (x' and λ') along the axes to x and λ expressed in meters. In Fig. 2d, x' and λ' correspond to the vertical and horizontal axes of the image (of WLI camera).

- Ordinate axis: By using the MgF_2 porthole without ITO (to avoid interference), an optical color filter corresponding to a wavelength λ is placed between the light source and the visible light beam splitter, which results in a horizontal bright stripe at λ'. Ten different filters are used, one at a time. Figure 5a shows the relationship $\lambda = a(\lambda' - 1) + \lambda_{min}$, where the slope $a = 0.1624\text{nm/px}$ represents the spectral resolution of our optical system. $\lambda_{min} = 437.24\text{nm}$ is the lowest visible wavelength. λ' ranges from 1 to 1280 px, which is the camera matrix vertical size. The visible spectrum bandwidth is then $\lambda_{min} \leq \lambda \leq \lambda_{max}$ where $\lambda_{ma} = 644.95\text{nm}$. The uncertainties on a and on λ are $\pm 0.002\text{nm/px}$ and $\pm 2.5\text{nm}$, respectively, for the confidence level of 95%.
- Abscissa axis is calibrated by imaging the square optical target with known dimensions printed on it. The spectrometer is used in mirror mode. Fig. 5b shows the calibration curve. x and x' are given in meters and pixels, respectively. The horizontal axis follows a relation in the form of $x = kx'$, where $k = 14.09\mu\text{m/px}$ is the spatial resolution. The linearity confirms the absence of optical distortions. The uncertainty of x' is one pixel size.

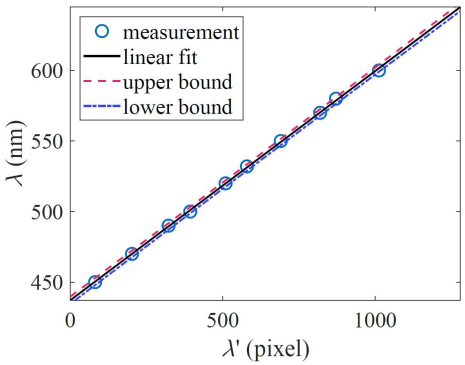

a) ***Relationship between camera vertical axis λ' and wavelength λ.***

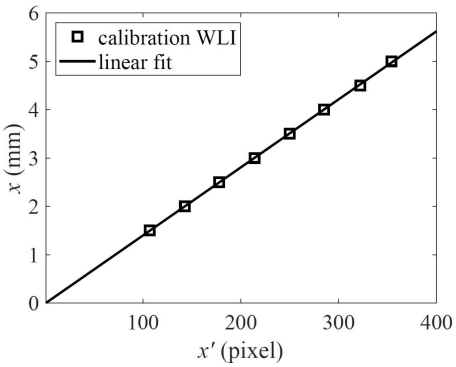

b) ***Relationship between camera horizontal axis x' and x along the scanning line.***

Figure 5. ***Calibration in white light interferometry.***

3.3. Image post-processing

We now describe the procedure to determine $\delta(x)$ for the boiling case (with ITO and bubble). We adopt the procedure proposed by Glovnea et al. [13]. In our boiling case, h and δ are both unknown. First, we obtain the ITO fringe map I_c at $t = 0$ corresponding to the frame just before the bubble nucleation. Only the interference fringe produced by h is then observed. $I_c = I(\lambda)/I_s(\lambda)$ is the fringe map that compensates the uneven intensity emission of the light source. $I_s(\lambda)$ is the spectral intensity of the LED light source, which is obtained with a bare MgF_2 (without ITO). We use the theoretical profile, $I_{c,theo}(\lambda)$, obtained by solving Eq. (1) to fit it to the experimental profile, $I_{c,exp}(\lambda)$. h is then determined by solving a problem where the function

$$F = \sum_{all\ \lambda} [I_{c,exp}(\lambda) - K I_{c,theo}(\lambda)]^2 \qquad (6)$$

is mimized. K is a scaling factor that accounts for the different intensity span in the measurements. The minimization is then solved for each point along x to get $h(x)$. A Levenberg-Marquardt algorithm is used to find $h(x)$ that minimizes F at x. For the images obtained during bubble growth, we proceed similarly. The fringe pattern is the one shown in Fig. 2d. The microlayer is recovered for all the images during the bubble lifetime to get $\delta(x,t)$. Figures 6 show examples of the fits between theoretical and experimental $I_c(\lambda)$ for the boiling case prior bubble nucleation without microlayer (Fig. 6a) and with microlayer (Fig. 6b). The good agreement between the between theoretical and experimental $I_c(\lambda)$ shows that h and δ are determined with high precision. The uncertainties on that h and δ are $\pm 10\text{nm}$. The advantage of this methodology is that an absolute measure of microlayer thickness is obtained. This is the first advantage of WLI in comparison with LI, which is only able to give a relative measure of the microlayer thickness.

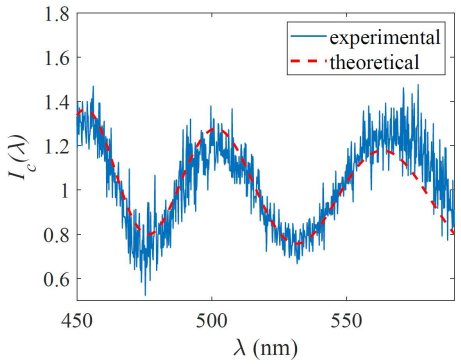

a) *Prior bubble nucleation.* $h = 944nm$.

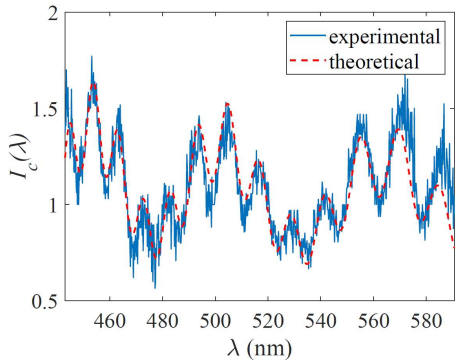

b) *After bubble nucleation.* $h = 944nm$ *and* $\delta = 6.48\mu m$

Figure 6. *Fits of theoretical* $I_c(\lambda)$ *to the experiment*.

3.4. Validation of the WLI microlayer measurement and comparison with LI

In order to validate the measurement of the microlayer thickness, we create a thin film layer of air by posing a lens over the flat porthole without ITO ($h = 0$), as illustrated in Fig. 7a. The fringe maps obtained in this case for WLI and LI are shown in Figs. 7b and 7c, respectively. The theoretical lens shape is known from its radius of curvature provided by the manufacturer. In this simple case, δ can be determined by counting the fringe sequential number N as

$$\delta = \frac{\lambda_{max,N}}{2n_3}(N - \Phi_{13}) \tag{7}$$

where $\lambda_{max,N}$ is the corresponding wavelength, for which the constructive interference occurs. Figure 7d depicts a comparison between the theoretical lens shape and the microlayer thickness recovered by LI and WLI. Both have a good agreement with the lens shape. However, WLI provides a higher thickness resolution, which shows its second advantage compared to LI. This is because thickness resolution in LI is $\lambda/4n_3$, which represents the spacing between two adjacent constructive and destructive fringes. In WLI, this limit no longer applies, thanks to the wavelength axis λ. The third advantage of WLI is that the geometry of a fringe in the WLI map corresponds to the film profile. This occurs because $\delta(x) \sim \lambda(x)$, Eq. (7), so one can have the microlayer shape qualitatively at once, without the need of post-processing. This is only possible thanks to the λ axis.

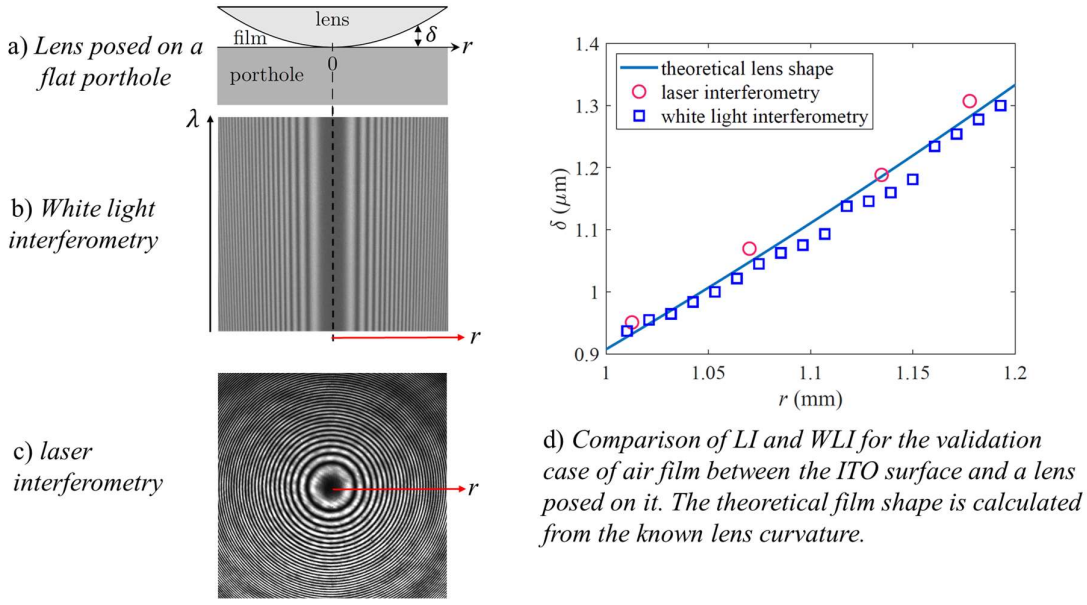

d) *Comparison of LI and WLI for the validation case of air film between the ITO surface and a lens posed on it. The theoretical film shape is calculated from the known lens curvature.*

Figure 7. ***Comparison between LI and WLI.***

4. INFRARED THERMOGRAPHY

4.1. Theory

The intensity I recorded by the IR camera is a measure of the wall temperature T_w. The IR radiation emitted from the ITO (Fig. 2) passes through the visible-IR beam splitter of the reflectance $R_{bs}(\lambda)$, the IR camera objective of the transmittance $T_{obj}(\lambda)$, and is registered by the IR camera sensor with the normalized response sensitiveness of $S_{det}(\lambda)$. Therefore, one writes

$$I(T_w) = \int_{\lambda 1}^{\lambda 2} R_{bs}(\lambda) S_{det}(\lambda) T_{obj}(\lambda) W^b(\lambda, T_w) d\lambda \tag{8}$$

where

$$W^b(\lambda, T_w) = \frac{C_1}{\lambda^5 \left[\exp\left(\frac{C_2}{\lambda T_w}\right) - 1\right]} \quad (9)$$

is the Plank's law. $C_1 = 3.74 \text{ x } 10^{-16}\,\text{W} \cdot \text{m}^2$ and $C_2 = 1.44 \text{ x } 10^{-2}\,\text{m} \cdot \text{K}$ represent the first and second radiation constants. $S_{det}(\lambda)$ and $T_{obj}(\lambda)$ were provided by the IR camera's manufacturer whereas $R_{bs}(\lambda)$ was determined experimentally by Fourier-Transform Infrared Spectroscopy [11]. The integration is performed for a wide range of T_w so one obtains $I = f(T_w)$. However, given that we measure I to obtain T_w, it is more appropriate to work with $T_w = f(I)$. As discussed in [14, 15] in a similar experimental work, the best fitting curve that relates $T_w(\text{K})$ to I is expressed as

$$T_w = A_1\left[(I + A_2)^{1/4} + A_3\right] \quad (10)$$

where A_1, A_2 and A_3 are fitting constants that account for the surrounding radiation, emissivity of the ITO and atmosphere attenuation. Figure 8a shows the integral of Plank's law (obtained via Eq. (9)) and the fit given by Eq. (10) for a wide range of T_w. The fit represents the integral of Plank's law with a root mean square error of 0.07 °C. Therefore, the formula expressed by Eq. (10) represents well the theory of Eq. (9) and one can use it for fitting the experimental calibration points.

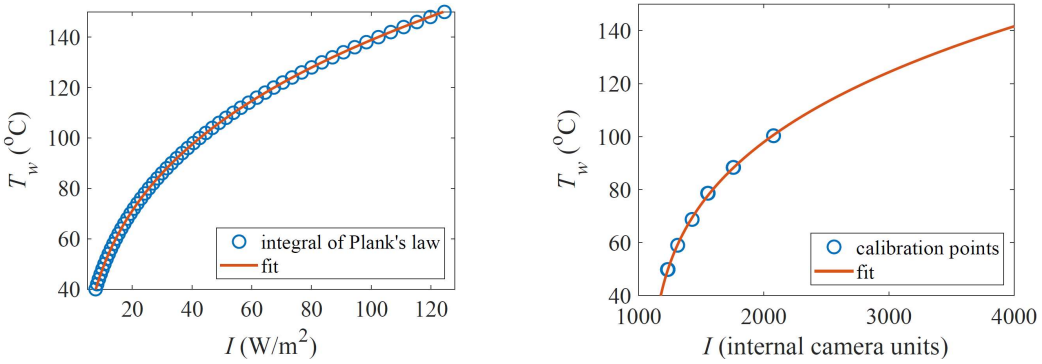

a) Fit with Eq. (10) of the theoretical Eq. (9). ***b) Fit with Eq. (10) of the camera signal.***

Figure 8. ***IR thermography calibration*****.**

4.2. Experiment

We use a pixel-wise calibration procedure [14, 15] to relate T_w with I so that each pixel has its own fitting coefficients. This is important to compensate the vignetting effect, for instance. Figure 8b shows the experimental calibration points for a given pixel. Six calibration points are obtained within the range $50°\text{C} \leq T_w \leq 100°\text{C}$. T_w is measured for the cell at thermal equilibrium with a resistance thermal detector (RTD) placed inside the water pool (Fig. 2). Equation (10) is used to fit the data. The fit represents the calibration points with a root mean square error of 0.4 K. One should note that the cell is at atmospheric pressure; calibration beyond the saturation temperature ($T_{sat} = 100°\text{C}$) is thus impossible. During the bubble growth, $T_w > T_{sat}$ and we need to extrapolate the calibration range. However, the error is expected to be minor thanks to the use of the physically justified fit.

5. RESULTS: SINGLE BUBBLE GROWTH AT NUCLEATE BOILING

5.1. Bubble nucleation, growth and departure

Figures 9 show the time evolution of the wall superheating $\Delta T = T_w - T_{sat}$ obtained by IRT at the bubble nucleation location. Figure 9a shows a few nucleation cycles with the blue-shaded area corresponding to the bubble growth period, which is expanded in Fig. 9b. The boiling cycles are periodical with approximately 248 ms between two consecutive bubble nucleation events. Because of the nucleation cycles periodicity (Fig. 9a), one can concentrate only on one of them.

The ΔT value required to overcome the nucleation energy barrier and trigger the bubble is $32\mathrm{K}$. In Fig. 9b, the bubble growth period, given by the time interval between bubble nucleation and departure from the wall, is $19\mathrm{ms}$. ΔT drops sharply at nucleation thanks to the wall heat removal promoted by the latent heat of vaporization. However, the rapid dry spot formation results in a sharp increase of ΔT. The ΔT increase slows-down after a few ms thanks to the radial heat diffusion (within the wall) towards the contact line. At bubble departure from the wall, ΔT decreases thanks to the wall rewetting by the cooler bulk liquid.

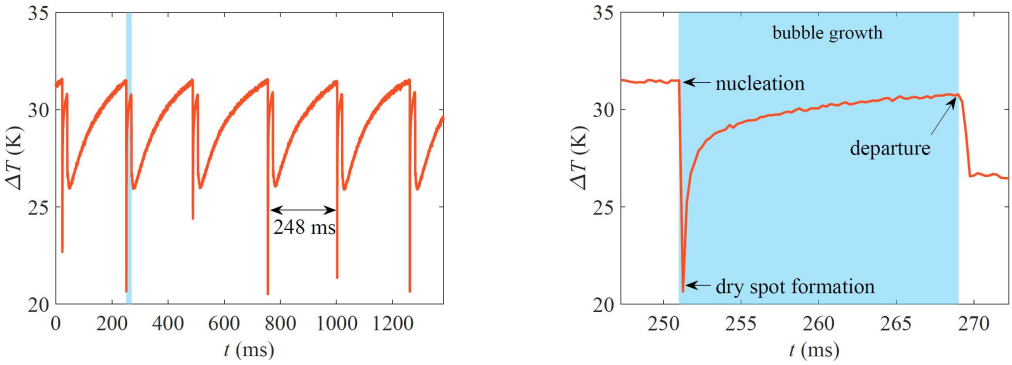

a) *Nucleation cycles.* **b) *Bubble growth.***

Figure 9. *Wall superheating evolution at the center of the bubble. The shaded zone indicates the bubble growth period.*

5.2. Bubble, dry spot and microlayer radii

The bubble equivalent radius $r_{b,eq}$ is obtained from the sidewide shadowgraphy, Fig. 2c. It corresponds to the radius that a sphere would have, with the same volume as the bubble. From WLI fringe images as those shown in Fig. 2d one identifies the dry spot r_{cl} and microlayer r_{μ} radii by the reflected light intensity. Figure 10a shows the time evolution of these radii. $t = 0$ ms corresponds to the moment just before nucleation; the bubble departs from the wall at $t = 19.5$ ms. For $0 \leq t \leq 1$ ms, the bubble and microlayer radii exhibit a similar dynamics controlled by the inertial bubble expansion, which results in a nearly hemispherical bubble shape. The microlayer radius attains 90% of its maximum $(2\mathrm{mm})$ within the first 10% of bubble growth period. The microlayer depletion occurs at $t = 12.5$ ms, when the dry spot and microlayer radii coincide. For $0 \leq t \leq 12.5$ ms, the microlayer exists and its evaporation contributes to the overall bubble growth. During the remaining bubble lifetime, the microlayer does not exist.

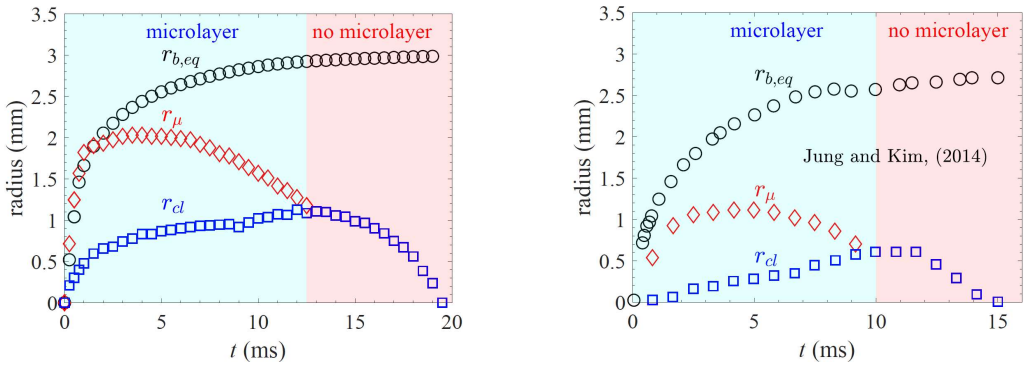

a) ***Local IR laser heating in the present experiment*** **b)** ***Joule heating regime data by Jung and Kim*** **[4].**

Figure 10. ***Temporal evolution of equivalent bubble radius $r_{b,eq}$, microlayer radius r_μ and dry spot (contact line) radius r_{cl}.***

The dynamics of $r_{b,eq}$, r_μ and r_{cl} shown in Fig. 10a is qualitatively similar to that obtained by Jung and Kim [4] (Fig. 10b) with the Joule (uniform) heating. Quantitatively, it can be noticed that r_μ is roughly two times larger in our case. This is related to the strength of the inertial forces acting during early moments of bubble expansion promoted by the laser heating. During the microlayer existence, r_{cl} has a linear behavior with Joule heating (Fig. 10b) whereas with laser heating (Fig. 10a) it grows faster for $0 \leq t \leq 2.5$ ms and then slows down for 2.5 ms $\leq t \leq 12.5$ ms, where it increases with a constant rate. This occurs because the wall superheating drives the contact line motion [16].

5.3. Microlayer dynamics

The microlayer thickness obtained by analyzing the WLI fringe map is shown in Fig. 2d. Because of the fast inertial dynamics at early stages of bubble growth, the fringes cannot be observed by WLI camera for $t < 1.25$ ms. For 8 ms $\leq t \leq 12.5$ ms, the width of the fringe pattern becomes too thin due the shortening of the microlayer extent (Fig. 10a), so the post-processing can no longer distinguish maxima and minima. Therefore, the experimental microlayer profile can only be obtained for 1.25 ms $\leq t \leq 8$ ms.

The experimental microlayer profile is shown in Fig. 11. The microlayer shape could be recovered only at a portion of its length (where the fringe pattern is visible) because in its other part, the interface slope is too big (or the optical resolution is insufficient, which is equivalent) so that the fringes are not visible. Interference fringes are only detectable for microlayer slopes lower than $\approx 0.4°$ [11] in our installation. We have evidenced [17] the dewetting phenomenon by means of numerical simulation. The liquid situated near the nucleation site is swept by the contact line receding, thus causing the wall dewetting [16]. Because of high viscous stresses in the film, the liquid cannot flow into the microlayer. Instead, it gets accumulated near the contact line thus creating there a dewetting ridge with high interfacial slopes, as illustrated in Fig. 1. A similar ridge occurred in several recent numerical simulations of nucleate pool boiling [18, 19, 20, 21]. The microlayer thins over time due to its evaporation, which contributes to the overall bubble growth.

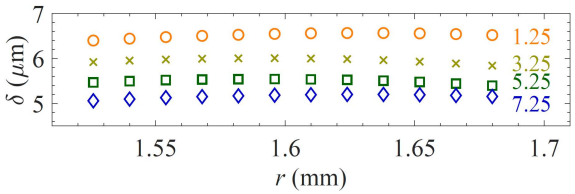

Figure 11. ***Microlayer thickness profile. The labels indicate the time in ms.***

5.4. Wall temperature

Figures 12a and 12b show $\Delta T(x, y)$ for $t = 0$ ms and $t = 6.25$ ms, respectively. In these figures, $(x = 0, y = 0)$ corresponds to the point on the wall where the bubble nucleation occurs. In Fig. 12a, one can understand the temperature distribution as a combination of the heat generation in the ITO provided by the IR laser heating, the heat diffusion towards the porthole and radial in the ITO and the convection into the liquid pool. In Fig. 12b, the presence of dry spot and microlayer change significantly this distribution. Therefore, we use $\Delta T(x, y, t = 0)$ as a reference to address how the microlayer and dry spot modify $\Delta T(x, y, t)$. For the sake of simplicity and due to nearly radial symmetry of the temperature distribution on the wall, as one can observe in Figs. 12a,b, the spatial distribution of ΔT can be studied by profiles of $\Delta T(x, t)$ at $y = 0$.

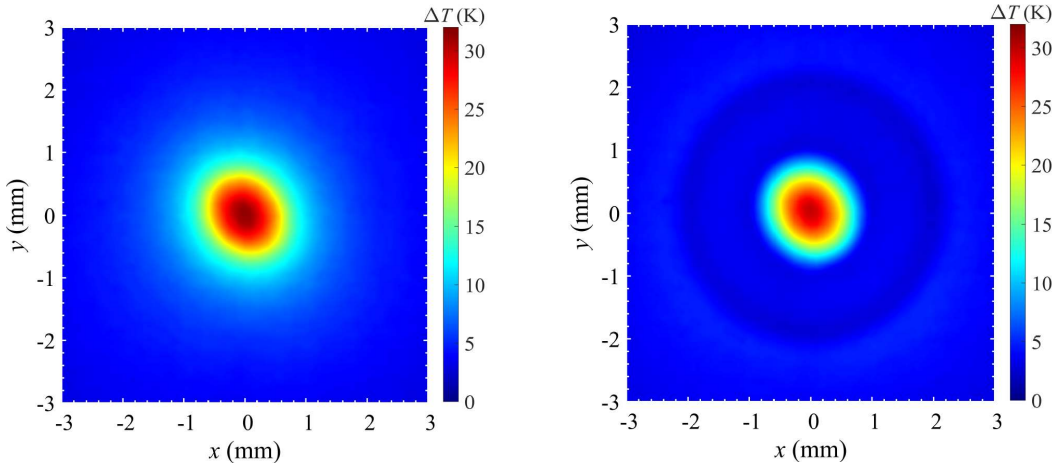

Figure 12. ***Wall superheating distribution wall.***

Figures 13a,b depict the wall superheating at the early stages of bubble growth. In Fig. 13a, we identify the extents of dry spot and microlayer along x as follows. As the microlayer is formed during the inertial bubble growth, evaporation of the liquid microlayer leads to a decrease of ΔT along its extent. Heat diffuses from the wall throughout the whole microlayer thickness within 0.25 ms, thus promoting an effective and rapid heat removal from the wall. As a result, the point where $\Delta T(t = 0.25\text{ms})$ starts to deviate from $\Delta T(t = 0)$ corresponds to the ending point $x = r_\mu$ of the microlayer (bubble foot edge). ΔT distribution is nonmonotonous inside the microlayer (Fig. 13a). This is a combined result of evaporation and nonuniform heating by the IR laser. While the high wall heat removal rate near the contact line works to decrease ΔT, the IR laser heating tends to increase it. The laser heating is maximum inside the dry spot thus producing high temperature gradients on the wall

in this region. As a result, we identify the dry spot radius $x = r_{cl}$ by two points where ΔT increases sharply. These points correspond to the contact line position.

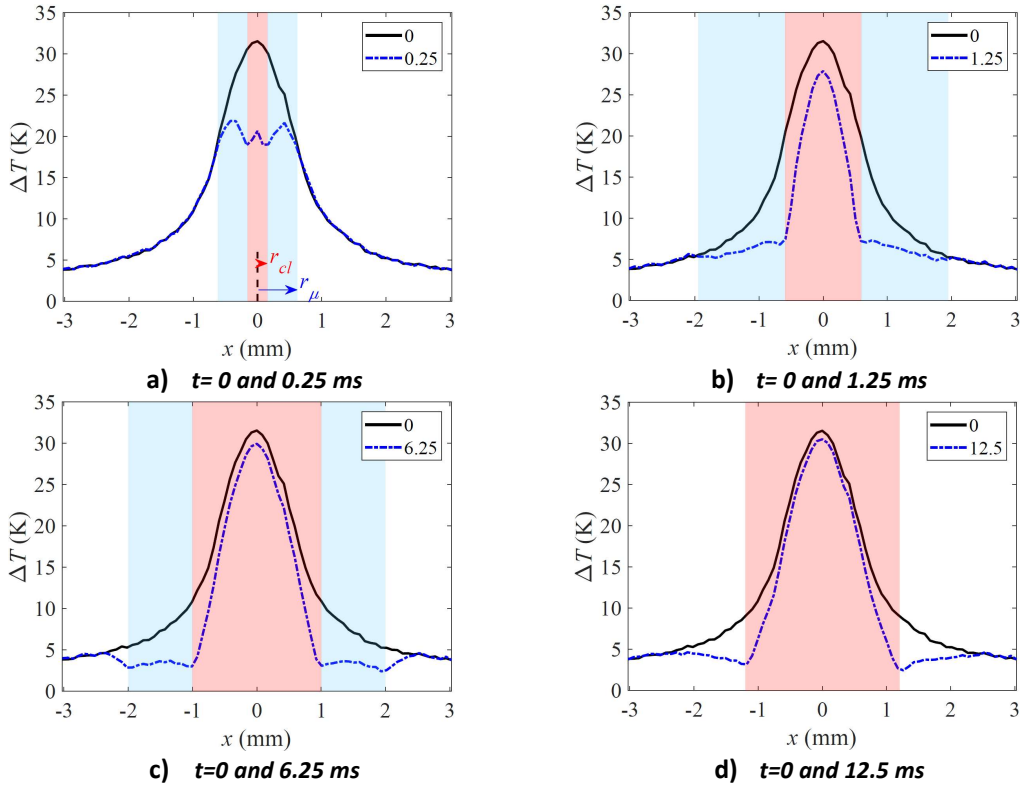

Figure 13. ***Spatial distributions $\Delta T(x)$ (blue dotted lines) for different time moments during the microlayer formation as compared to $\Delta T(x, t = 0)$ (black lines). The shaded areas represent the extents of dry spot (in red) and of microlayer (in blue).***

As one can observe in Figs. 13, $\Delta T(t)$ is a decreasing function along the whole extent of the microlayer as the bubble grows. In particular, at $t = 1.25$ ms, $\Delta T(x)$ is nearly uniform inside the microlayer thus conforming the effective wall cooling along its extent. Over the dry spot, the temperature profile follows approximately the shape of that at $t = 0$. As the microlayer approaches its full extent (at $t = 1.25\text{ms}$), the changes in ΔT along the dry spot become minor. This is a result of the effective wall heat removal at the contact line and also throughout the whole microlayer extent.

Figure 13c shows the ΔT distribution after the microlayer is fully developed. Here, its variariation is different. ΔT inside microlayer is lower than at its periphery. As a result, heat diffuses inwards. The point where the profiles for t =0 and 6.25 ms start to deviate from each other no longer corresponds to r_μ. Instead, at $r_\mu = 2\text{mm}$ and at $r_{cl} = 1\text{mm}$ we have two ΔT minima; the region between them corresponds to the microlayer. The minima at $x = \pm 2\text{mm}$ correspond to the cold ring on the $x - y$ map of Fig. 12b. When the microlayer is depleted at $t = 12.5\text{ms}$ in Fig. 13d, the second pair of minima of ΔT at $x = \pm 2\text{mm}$ disappears. For $t > 12.5\text{ms}$, the temperature at the contact line increases due to the absence of microlayer.

These wall temperature distributions provide relevant information to understand the role of microlayer and dry spot on the microlayer evaporation and the dewetting dynamics. Moreover, the data can also be used to determine the wall heat flux and study the interfacial thermal resistance [11].

6. CONCLUSIONS

In this work, we present novel high-speed and high-resolution optical techniques for near-wall investigations at bubble growth in nucleate boiling. White light interferometry, infrared thermography and sidewise shadowgraphy are used to measure the microlayer thickness, the wall temperature and the bubble macroscopic shape, respectively. Unlike laser interferometry, white light interferometry provides absolute microlayer thickness with high precision and higher thickness resolution. It also allows the detection of dry spot, so the dewetting dynamics can be studied. We show that insightful data can be obtained during the bubble growth on a heated wall with these optical techniques, which can be used to gain the fundamental understanding of the near-wall boiling heat transfer phenomena.

7. REFERENCES

[1] T. N. Dinh and T. G. Theofanous, "Nucleation phenomena in boiling," *Multiphase Sci. Technol.,* vol. 15, pp. 349-363, 2003.

[2] T. G. Theofanous, "The boiling crisis in nuclear reactor safety and performance," *Int. J. Multiphase Flow,* vol. 6, pp. 69-95, 1980.

[3] L. Zhang, J. H. Seong and M. Bucci, "Percolative scale-free behavior in the boiling crisis," *Phys. Rev. Lett.,* vol. 122, p. 134501, 2019.

[4] S. Jung and H. Kim, "An experimental method to simultaneously measure the dynamics and heat transfer associated with a single bubble during nucleate boiling on a horizontal surface," *Int. J. Heat Mass Transfer,* vol. 73, pp. 365-375, 2014.

[5] V. S. Nikolayev and D. A. Beysens, "Boiling crisis and non-equilibrium drying transition," *Europhys. Lett.,* vol. 47, pp. 345-351, 1999.

[6] V. Janeček and V. S. Nikolayev, "Triggering the boiling crisis: a study of the dry spot spreading mechanism," *Interfacial Phenom. Heat Transf.,* vol. 2, pp. 363-383, 2014.

[7] Z. Chen, A. Haginiwa and Y. Utaka, "Detailed structure of microlayer in nucleate pool boiling for water measured by laser interferometric method," *Int. J. Heat Mass Transfer,* vol. 108, pp. 1285-1291, 2017.

[8] G. K. Sinha, S. Narayan and A. Srivastava, "Microlayer dynamics during the growth process of a single vapour bubble under subcooled flow boiling conditions," *J. Fluid Mech.,* vol. 931, p. A23, 2022.

[9] M. Gao, L. Zhang, P. Cheng and X. Quan, "An investigation of microlayer beneath nucleation bubble by laser interferometric method," *Int. J. Heat Mass Transfer,* vol. 57, pp. 183-189, 2013.

[10] S. Jung and H. Kim, "An experimental study on heat transfer mechanisms in the microlayer using integrated total reflection, laser interferometry and infrared thermometry technique," *Heat Transfer Eng.,* vol. 36, pp. 1002-1012, 2015.

[11] C. Tecchio, "Experimental study of boiling: Characterization of near-wall phenomena and bubble dynamics," 2022.

[12] H. A. MacLeod, Thin-film optical filters, 3rd ed., CRC Press, 2010.

[13] R. P. Glovnea, A. K. Forrest, A. V. Olver and H. A. Spikes, "Measurement of sub-nanometer lubricant films using ultra-thin film interferometry," *Tribol. Lett.,* vol. 15, pp. 217-230, 2003.

[14] A. Sielaff, "Experimental investigation of single bubbles and bubble interactions in nucleate boiling," 2014.

[15] K. Schweikert, A. Sielaff and P. Stephan, "Pixel-wise in situ calibration method for high accuracy infrared thermography of moving targets," *Infrared Phys. Technol.,* vol. 118, p. 103862, 2021.

[16] X. Zhang and V. S. Nikolayev, "Dewetting acceleration by evaporation," *J. Fluid Mech.,* vol. 948, p. A49, 2022.

[17] C. Tecchio, X. Zhang, B. Cariteau, G. Zalczer, P. Roca i Cabarrocas, P. Bulkin, J. Charliac, S. Vassant and V. Nikolayev, "Microlayer dynamics at bubble growth in boiling," in *Proc. 16th Int. Conf. Heat Transfer Fluid Mech. Thermodynamics (HEFAT-ATE 2022)*, 2022.

[18] G. Giustini, "Hydrodynamic analysis of liquid microlayer formation in nucleate boiling of water," *Int. J. Multiphase FLow,* vol. 172, p. 104718, 2024.

[19] A. Urbano, S. Tanguy, G. Huber and C. Colin, "Direct numerical simulation of nucleate boiling in micro-layer regime," *Int. J. Heat Mass Transfer,* vol. 123, pp. 1128-1137, 2018.

[20] L. Bureš and Y. Sato, "On the modelling of the transition between contact-line and microlayer evaporation regimes in nucleate boiling," *J. Fluid Mech.,* vol. 916, p. A53, 2021.

[21] A. Guion, S. Afkhami, S. Zaleski and J. Buongiorno, "Simulations of microlayer formation in nucleate boiling," *Int. J. Heat Mass Transfer,* vol. 127, pp. 1271-1284, 2018.